Particle Accelerators, 1987, Vol. 20, pp. 239–265
0031-2460/87/2004–0239/$25.00/0

Printed in the United States of America

TRIANGULAR DISCRETIZATION METHOD FOR THE EVALUATION OF RF FIELDS IN WAVEGUIDES AND CYLINDRICALLY SYMMETRIC CAVITIES

U. VAN RIENEN and T. WEILAND

Deutsches Elektronensynchrotron (DESY), Notkestr. 85, 2000 Hamburg 52, Federal Republic of Germany

(Received in final form January 15, 1986)

The design of rf accelerating structures nowadays is largely based on mesh codes that solve for fields and eigenfrequencies in arbitrarily shaped cavities. The most developed codes deal with structures of cylindrical symmetry. However, no program is available that can solve for fields with azimuthal variation in cavities with dielectric and/or permeable insertions. Here we describe a discretization method using an "orthogonal triangular double grid." The special mesh and the FIT discretization allow the treatment of cavities and waveguides with arbitrary material insertions and combines the features of SUPERFISH (triangular mesh, rotationally symmetric fields) and URMEL (rectangular mesh but fields with or without azimuthal variation).

1. INTRODUCTION

1.1. Cylindrical Cavities

In cavities of cylindrical symmetry, the electromagnetic fields are periodic in the azimuthal variable (φ) with period 2π. This fact and the harmonic time dependence of the fields allow their description by a Fourier series:

$$\begin{aligned}\underline{\mathbf{F}}(r, \varphi, z, t) = \sum_{m=0}^{\infty} \mathrm{Re}\,\{[&\underline{F}_r(r, z)e^{im\varphi}\mathbf{e}_r \\ &+ \underline{F}_\varphi(r, z)e^{im\varphi}\mathbf{e}_\varphi \\ &+ \underline{F}_z(r, z)e^{im\varphi}\mathbf{e}_z]e^{i\omega t}\},\end{aligned} \tag{1}$$

with the complex magnitude $\underline{\mathbf{F}} = \underline{\mathbf{E}}$ or $\underline{\mathbf{H}}$ and the unit vectors $\mathbf{e}_r$, $\mathbf{e}_\varphi$, $\mathbf{e}_z$ in the r, φ, z directions. A list of symbols follows the reference list. Furthermore, the materials are assumed loss free, i.e., ϵ, μ are real and the conductivity is equal to zero. So we may write

$$\begin{aligned}\mathbf{E} &= \sqrt{Z_0}\sin\omega t\mathbf{E}', \\ \mathbf{H} &= \sqrt{Y_0}\cos\omega t\mathbf{H}',\end{aligned} \tag{2}$$

with $Z_0 = \sqrt{\mu_0/\epsilon_0}$, $Y_0 = \sqrt{\epsilon_0/\mu_0}$, $c = 1/\sqrt{\mu_0\epsilon_0}$.

Then Maxwell's equations are given by

$$\begin{aligned} \operatorname{curl} \mathbf{H}' &= \epsilon_r \frac{\omega}{c} \mathbf{E}', \\ \operatorname{curl} \mathbf{E}' &= \mu_r \frac{\omega}{c} \mathbf{H}'. \end{aligned} \tag{3}$$

The azimuthal dependence $e^{im\varphi}$ leads to several groups of modes:

(i) $m = 0$: "TE" or "H" modes with $\mathbf{E} = (0, E_\varphi, 0)$,
(ii) $m = 0$: "TM" or "E" modes with $\mathbf{H} = (0, H_\varphi, 0)$ (accelerating modes),
(iii) $m > 0$: these so called deflecting or transverse modes are excited by off-axis particles.

1.2. Waveguides

In waveguides which don't change their characteristics in the z direction (using Cartesian coordinates), waves with a pure exponential dependence on z are proper solutions of Maxwell's equations. Consequently, we may write for waves traveling in the negative direction

$$\begin{aligned} \underline{\mathbf{F}}(x, y, z, t) = \operatorname{Re} \{ & [\underline{F}_x(x, y) e^{i\beta z} \mathbf{e}_x \\ & + \underline{F}_y(x, y) e^{i\beta z} \mathbf{e}_y \\ & + \underline{F}_z(x, y) e^{i\beta z} \mathbf{e}_z] e^{i\omega t} \}, \end{aligned} \tag{4}$$

with the Cartesian unit vectors $\mathbf{e}_x$, $\mathbf{e}_y$, $\mathbf{e}_z$.

With

$$\begin{aligned} \mathbf{E} &= \sqrt{Z_0} \sin \omega t \mathbf{E}', \\ \mathbf{H} &= \sqrt{Y_0} \cos \omega t \mathbf{H}', \end{aligned} \tag{5}$$

we get for Maxwell's equations

$$\begin{aligned} \operatorname{curl} \mathbf{H}' &= \epsilon_r \frac{\omega}{c} \mathbf{E}', \\ \operatorname{curl} \mathbf{E}' &= \mu_r \frac{\omega}{c} \mathbf{H}'. \end{aligned} \tag{6}$$

2. DISCRETIZATION

Because of the cylindrical symmetry of the cavity (that is, the z independence of the waveguide shape), a two-dimensional grid is sufficient (see Fig. 1). As we will see, the azimuthal dependence or the z dependence of the fields can be taken out of the numerical computation (compare Refs. 1–3). The basic ideas of the FIT method have been transferred to a triangular mesh. This mesh has the advantage of approximating well the cavity or waveguide geometry, even for elliptical or circular structures, with relatively coarse grids (see Figs. 2 and 3).

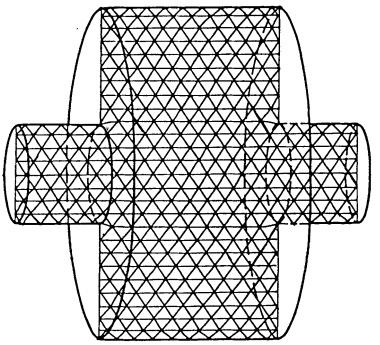

FIGURE 1 Pillbox cavity with triangular mesh.

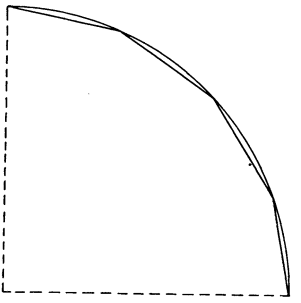

FIGURE 2 Approximation to a circular geometry with a triangular mesh ($N = 16$ mesh points).

2.1. *Allocation of the Field Components to the Grid*

In the rectangular mesh of URMEL[2,4] the field components E_r, E_φ, E_z of $\mathbf{E}'$ and H_r, H_φ, H_z of $\mathbf{H}'$ (or correspondingly, E_x, E_y, E_z of $\mathbf{E}'$ and H_x, H_y, H_z of $\mathbf{H}'$) are represented as shown in Fig. 4. Two dual grids are used—one for the electric and one for the magnetic field components. Different components associated with one mesh point are allocated at different locations of the grid. The characteristic and

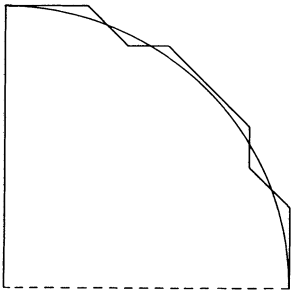

FIGURE 3 Approximation to a circular geometry with a rectangular mesh, using also diagonals ($N = 64$ mesh points).

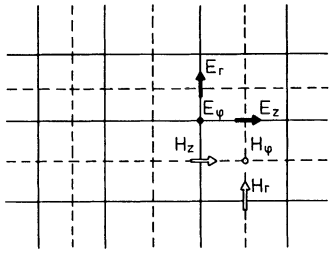

FIGURE 4 Rectangular mesh and its dual mesh with E_r, E_φ, E_z and H_r, H_φ, H_z.

the advantage of this allocation is the preservation of the interrelation between the integrals over areas and the line integrals in Maxwell's equations. For the triangular mesh, we proceed in an analogous way.

But here we must distinguish two cases:

(i) If all triangles of the mesh inside the cavity have angles less than or equal to $\pi/2$, we choose as dual mesh lines the perpendicular bisectors of the sides (see Figs. 5 and 6). These intersect in the center of a circle drawn through the three vertices of the triangle.

(ii) The program starts with a mesh of regular triangles and varies it in order to approximate the given boundaries as well as possible. In this process, it cannot always avoid triangles with an angle larger than $\pi/2$. If this happens, the use of the above-defined dual mesh points would lead to the following problem: Some dual mesh points are outside the proper triangles (Fig. 7). In this case we use the centers of mass as dual mesh points.

It should be noted that the $\tilde{\mathbf{F}}$ component in this dual mesh is in general not perpendicular to the $\mathbf{F}$ component (see Fig. 8).

In the following, we will denote the dual mesh with perpendicular bisectors for sides as $\mathbf{G_M}$, that with centers of mass as $\mathbf{G_S}$, and the triangular mesh as $\mathbf{G}$. The numbering of mesh points and the allocation of the triangles to these points is explained in the following. The numbering of the mesh points is done analogously to URMEL, as may be seen in Fig. 9. This picture also demonstrates that there are two kinds of triangles alternating in the rows: One has the vertex on top,

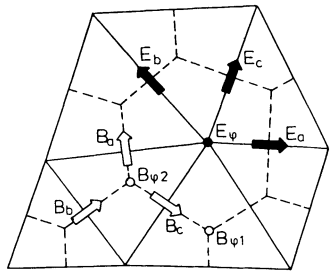

FIGURE 5 Triangular mesh and its dual (hexagonal) mesh with E_a, E_b, E_c, E_φ and B_a, B_b, B_c, B_{φ_1}, B_{φ_2}.

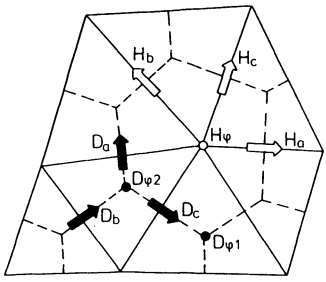

FIGURE 6 Triangular mesh with dual mesh and H_a, H_b, H_c, H_φ, D_a, D_b, D_c, D_{φ_1}, D_{φ_2}.

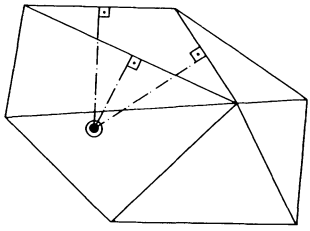

FIGURE 7 An obtuse triangle, showing that the center of the circumscribed circle lies outside the triangle.

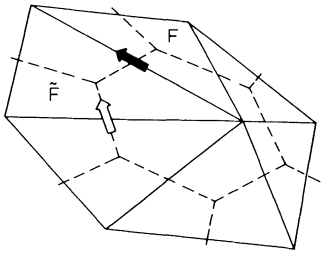

FIGURE 8 Dual mesh with centers of mass as mesh points; $(F, \tilde{F}) = (E, B)$ or (H, D).

while the other one is standing upright. One of each kind is associated with each mesh point k $[k = (j-1) \cdot J + i$ with $j = 1, \ldots, J$, $i = 1, \ldots, I]$. The triangle of the first kind is named $(1, k)$ and the second $(2, k)$. As Fig. 9 demonstrates, the order of the triangles starts with one of the first kind in the rows with an odd j and with one of the second kind in all rows with an even j.

Figure 10 shows for a general mesh point k all adjacent triangles, triangle sides, and mesh points. Evidently, a part of this is absent for boundary points. In some places in the formulas, in the following sections and in the appendix, superposed indices are used. The upper one always refers to the formula for a point $k = (j-1) \cdot J + i$ in row j with even j (type I), while the lower one refers to the formula for k in row j with odd j (type II). The allocation of all the field components, associated with a mesh point, is illustrated in Fig. 11 for the points l of type I and k of type II.

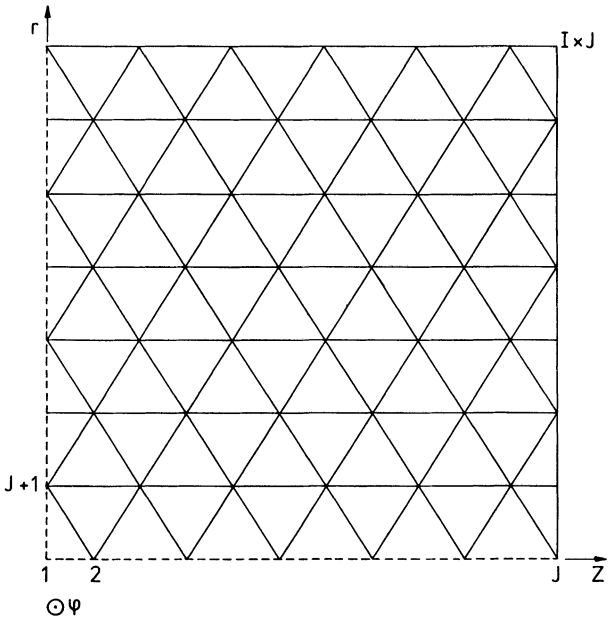

FIGURE 9 Numbering of the mesh points.

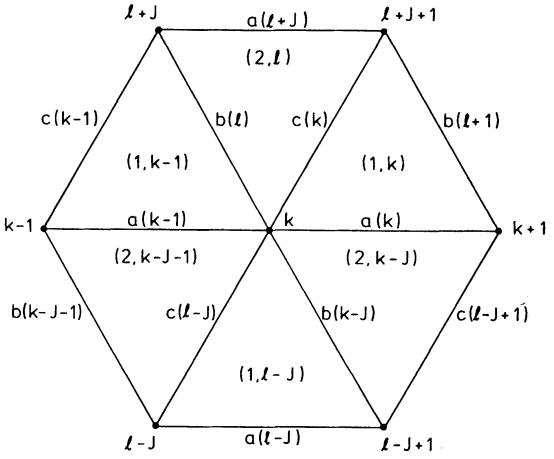

with $k = (j-1)\cdot J + i$

and $\ell = \begin{Bmatrix} k \\ k-1 \end{Bmatrix}$ for $\begin{Bmatrix} j & \text{even} \\ j & \text{odd} \end{Bmatrix}$

FIGURE 10 Points, sides, and triangles adjacent to a mesh point.

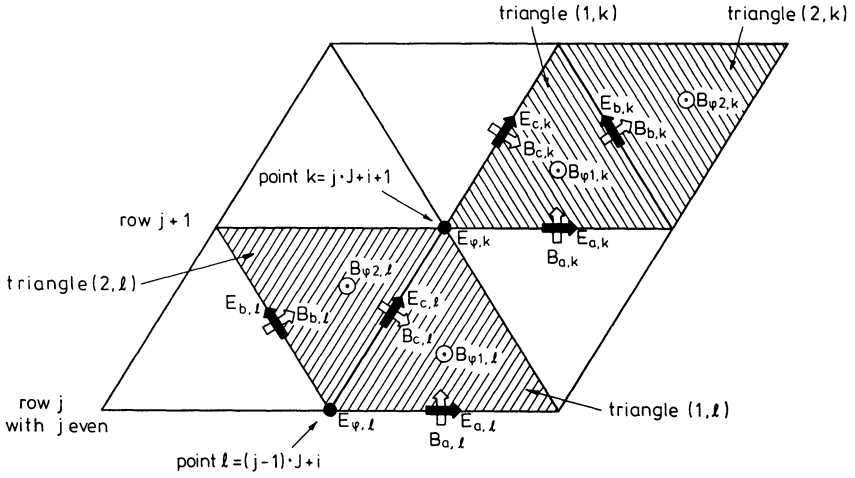

FIGURE 11 Location of the field components and the triangles associated with one mesh point.

2.2. *Allowed Material Properties in the Different Grids*

As mentioned above, the permittivity and the permeability shall be real. For $\mathbf{G_M}$ as dual mesh, any inserted material may have $\mu_r \neq 1$ and $\epsilon_r \neq 1$ and either E or H could be chosen for F (see Figs. 12 and 13). In Fig. 12, it may be seen that only continuous components (i.e., tangential E and normal B) occur, so that triangles of $\mathbf{G}$ may be filled with materials with $\mu_r \neq 1$ and $\epsilon_r \neq 1$ and varying from triangle to triangle. Similarly, in Fig. 13, only tangential H and normal D occur at the triangle boundaries.

If only the dual mesh $\mathbf{G_S}$ can be used, we have to place a restriction to assure the continuity of the field components: Only insertions with $\mu_r \neq 1$ but $\epsilon_r = 1$, or $\epsilon_r \neq 1$ but $\mu_r = 1$ are allowed, and F will be taken as shown in Figs. 14 and 15. In Fig. 14, it is seen that (continuous) tangential E occurs at the triangle interfaces, and so ϵ_r can vary from triangle to triangle. However, since on the dual mesh the magnetic field component is not normal to the interfaces, μ_r can not vary from

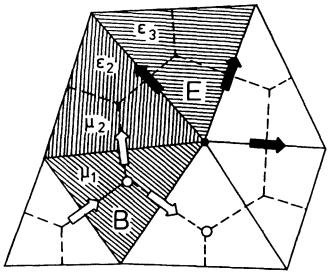

FIGURE 12 E on $\mathbf{G}$, B on $\mathbf{G_M}$, $\mu_r \neq 1$, $\epsilon_r \neq 1$.

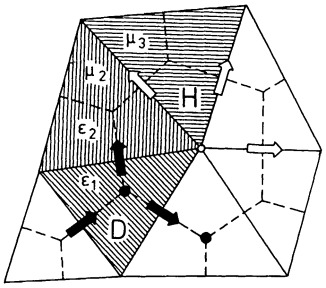

FIGURE 13 H on $\mathbf{G}$, D on $\mathbf{G_M}$, $\mu_r \neq 1$, $\epsilon_r \neq 1$.

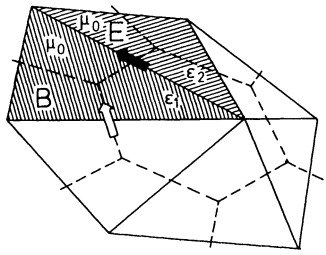

FIGURE 14 E on $\mathbf{G}$, B on $\mathbf{G_S}$, $\mu = \mu_0$, $\epsilon_r \neq 1$.

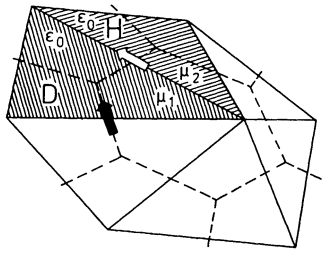

FIGURE 15 H on $\mathbf{G}$, D on $\mathbf{G_S}$, $\mu_r \neq 1$, $\epsilon = \epsilon_0$.

triangle to triangle. Similarly, in Fig. 15, it can be seen that, with H on the mesh $\mathbf{G}$, μ_r can vary whereas ϵ_r cannot.

Although the constants μ_0 and ϵ_0 are shown in Figs. 14 and 15, in fact if the cavity or waveguide were completely filled with a medium with constant μ_r or constant ϵ_r, respectively, only continuous field components would occur. However, for nearly all structures, it is possible to find a mesh which renders $\mathbf{G_M}$ possible as a dual mesh.

2.3. *Deflecting Modes, $m > 0$*

With the given assumptions, the electromagnetic fields can be written as

$$\begin{aligned}\mathbf{E}(r, \varphi, z, t) = \sqrt{Z_0} \sin \omega t \sum_{m=0}^{\infty} [&E_{m,r}(r, z) \cos m\varphi \mathbf{e}_r \\ &+ E_{m,\varphi}(r, z) \sin m\varphi \mathbf{e}_\varphi \\ &+ E_{m,z}(r, z) \cos m\varphi \mathbf{e}_z], \end{aligned} \tag{7}$$

$$\begin{aligned}\mathbf{H}(r, \varphi, z, t) = \sqrt{Y_0} \cos \omega t \sum_{m=0}^{\infty} [&H_{m,r}(r, z) \sin m\varphi \mathbf{e}_r \\ &+ H_{m,\varphi}(r, z) \cos m\varphi \mathbf{e}_\varphi \\ &+ H_{m,z}(r, z) \sin m\varphi \mathbf{e}_z]. \end{aligned} \tag{8}$$

As in Eq. (2), we will use $\mathbf{E}'$ and $\mathbf{H}'$. For $(\mathbf{F}', \tilde{\mathbf{F}}') = (\mathbf{H}', \mathbf{D}')$ we choose $\varphi = \varphi + \pi/2$ in Eqs. (7) and (8). For each azimuthal mode number m, Maxwell's

equations in integral form then read as

$$\begin{aligned}
\oint \mathbf{H}' \cdot d\mathbf{s} &= \frac{w}{c} \int \epsilon_r \mathbf{E}' \cdot d\mathbf{A}, \\
\oint \mathbf{E}' \cdot d\mathbf{s} &= \frac{\omega}{c} \int \mu_r \mathbf{H}' \cdot d\mathbf{A}, \\
\iint \epsilon_r \mathbf{E}' \cdot d\mathbf{A} &= 0, \\
\iint \mu_r \mathbf{H}' \cdot d\mathbf{A} &= 0.
\end{aligned} \tag{9}$$

These equations are solved for a chosen $m > 0$ in the following way:

(i) They are discretized on the triangular mesh $\mathbf{G}$ with $\mathbf{G_S}$ (or $\mathbf{G_M}$) for $(\mathbf{F}', \tilde{\mathbf{F}}') = (\mathbf{E}', \mathbf{B}')$ or $(\mathbf{H}', \mathbf{D}')$. The boundary conditions are implied in the discretization. The details are given in the appendix.

(ii) In the resulting equations all $\tilde{\mathbf{F}}'$ components and the azimuthal $\mathbf{F}'$ component F_φ are eliminated. This leads to a linear algebraic eigenvalue problem connecting each field component F_a, F_b, F_c with ten neighbors:

$$\begin{aligned}
\left(\frac{\omega}{c}\right)^2 F_{a,k} = {} & \alpha_{aa,k,0} F_{a,k} \\
& + \alpha_{aa,k,1} F_{a,k+1} + \alpha_{aa,k,2} F_{a,k-1} \\
& + \alpha_{ab,k,0} F_{b,k} + \alpha_{ab,k,1} F_{b,k\pm 1} \\
& + \alpha_{ab,k,2} F_{b,k-J+1} + \alpha_{ab,k,3} F_{b,k-J} \\
& + \alpha_{ac,k,0} F_{c,k} + \alpha_{ac,k,1} F_{c,k+1} \\
& + \alpha_{ac,k,2} F_{c,k-J\pm 1} + \alpha_{ac,k,3} F_{c,k-J}
\end{aligned} \tag{10}$$

$$\begin{aligned}
\left(\frac{\omega}{c}\right)^2 F_{b,k} = {} & \alpha_{bb,k,0} F_{b,k} \\
& + \alpha_{bb,k,1} F_{b,\substack{k+J-1 \\ k+J}} + \alpha_{bb,k,2} F_{b,\substack{k-J \\ k-J+1}} \\
& + \alpha_{ba,k,0} F_{a,k} + \alpha_{ba,k,1} F_{a,k+J} \\
& + \alpha_{ba,k,2} F_{a,k+J-1} + \alpha_{ba,k,3} F_{a,k\mp 1} \\
& + \alpha_{bc,k,0} F_{c,k} + \alpha_{bc,k,1} F_{c,k+J} \\
& + \alpha_{bc,k,2} F_{c,k\mp 1} + \alpha_{bc,k,3} F_{c,k-J}
\end{aligned} \tag{11}$$

$$\begin{aligned}
\left(\frac{\omega}{c}\right)^2 F_{c,k} = {} & \alpha_{cc,k,0} F_{c,k} \\
& + \alpha_{cc,k,1} F_{c,\substack{k+J+1 \\ k+J}} + \alpha_{cc,k,2} F_{c,\substack{k-J \\ k-J-1}} \\
& + \alpha_{ca,k,0} F_{a,k} + \alpha_{ca,k,1} F_{a,k+J\pm 1} \\
& + \alpha_{ca,k,2} F_{a,k+J} + \alpha_{ca,k,3} F_{a,k-1} \\
& + \alpha_{cb,k,0} F_{b,k} + \alpha_{cb,k,1} F_{b,k+J} \\
& + \alpha_{cb,k,2} F_{b,k\pm 1} + \alpha_{cb,k,3} F_{b,k-J}
\end{aligned} \tag{12}$$

This relation between the field components is schematically illustrated in Fig. 16.

Equations (10) through (12), which are given for every mesh point k, correspond in their matrix representation to a linear algebraic eigenvalue problem. Thus, an eigenvalue problem

$$A\mathbf{x} = k^2\mathbf{x}, \quad \text{with the wave number } k = \frac{\omega}{c}, \tag{13}$$

remains to be solved. Its eigenvalues are the squared wave numbers of the resonant frequencies, and the eigenvectors

$$\mathbf{x} = (F_{a,1}, \ldots, F_{a,N}, F_{b,1}, \ldots, F_{b,N}, F_{c,1}, \ldots, F_{c,N})^T$$

give the corresponding electric and magnetic fields. Here an advantage of the FIT method becomes obvious: While other methods (e.g., SUPERFISH,[5] PRUD[6]) don't solve a linear problem and need an estimation of the frequency sought, this method solves a linear problem for which the solution gives the resonant frequencies. Since pure TE and TM modes (see Section 2.4) exist as deflecting modes only for the pillbox cavity, all six field components have to be calculated.

The matrix of the eigenvalue problem is sparse and the nonzero elements lie on a few off-diagonals, as shown in Fig. 17. The matrix is $3N \times 3N$.

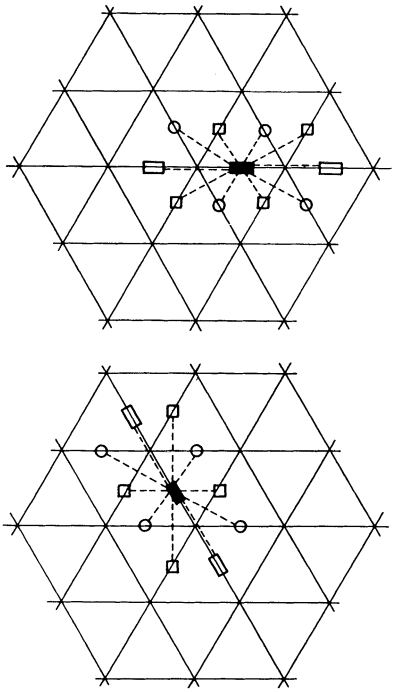

FIGURE 16 Illustration of the connection to ten neighbors by the difference equations for $F_{a,k}$ (upper figure) and $F_{b,k}$.

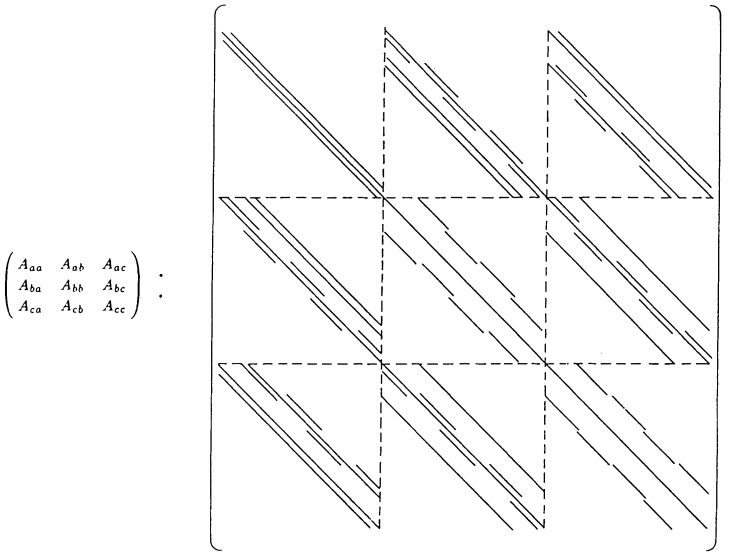

FIGURE 17 Matrix of the eigenvalue problem for $m > 0$.

2.4. *Monopole Modes*, $m = 0$

Here we have to distinguish two classes of modes: TEO modes: transverse electric fields with $E_z = 0$; $E_r = 0$; $H_\varphi = 0$; H_r, H_z, and E_φ have to be calculated. TMO modes: transverse magnetic fields with $H_z = 0$; $H_r = 0$; $E_\varphi = 0$; E_r, E_z, and H_φ are calculated.

Maxwell's equations [Eq. (9)] are solved for $m = 0$ as follows:

(i) They are discretized on the triangular mesh with $(\mathbf{F}', \tilde{\mathbf{F}}') = (\mathbf{E}', \mathbf{B}')$ for TM modes and $(\mathbf{F}', \tilde{\mathbf{F}}') = (\mathbf{H}', \mathbf{D}')$ for TE modes. (See appendix for details.)

(ii) In the resulting equations all $\mathbf{F}'$ components are eliminated. $\tilde{F}_{\varphi 1}$ and $\tilde{F}_{\varphi 2}$ are the only nonzero $\tilde{\mathbf{F}}'$-components. Again, we obtain a linear eigenvalue problem—in this case connecting each field component $\tilde{F}_{\varphi 1}$ and $\tilde{F}_{\varphi 2}$ with three neighbors:

$$\left(\frac{\omega}{c}\right)^2 \tilde{F}_{\varphi 1,k} = \alpha_{11,k,0}\tilde{F}_{\varphi 1,k} + \alpha_{12,k,0}\tilde{F}_{\varphi 2,k} + \alpha_{12,k,1}\tilde{F}_{\varphi 2,k\pm 1} + \alpha_{12,k,2}\tilde{F}_{\varphi 2,k-J} \tag{14}$$

$$\left(\frac{\omega}{c}\right)^2 \tilde{F}_{\varphi 2,k} = \alpha_{22,k,0}\tilde{F}_{\varphi 2,k} + \alpha_{21,k,0}\tilde{F}_{\varphi 1,k} + \alpha_{21,k,1}\tilde{F}_{\varphi 1,k\mp 1} + \alpha_{21,k,2}\tilde{F}_{\varphi 1,k+J} \tag{15}$$

Figure 18 shows a schematic representation of the relation expressed in (14) and (15). As for $m > 0$, a linear eigenvalue problem [Eq. (13)] is to be solved. The

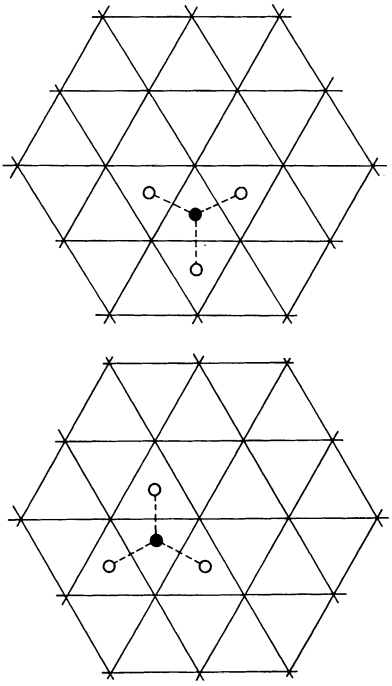

FIGURE 18 Connection of $\tilde{F}_{\varphi_1}$ (upper figure) and $\tilde{F}_{\varphi_2}$ to three neighbors by the difference equations.

eigenvectors are now

$$\mathbf{x} = (\tilde{F}_{\varphi 1,1}, \ldots, \tilde{F}_{\varphi 1,N}, \tilde{F}_{\varphi 2,1}, \ldots, \tilde{F}_{\varphi 2,N})^T.$$

The $2N \times 2N$ matrix $\mathbf{A}$ is sparse, can be made symmetric, and has only some off-diagonals (see Fig. 19).

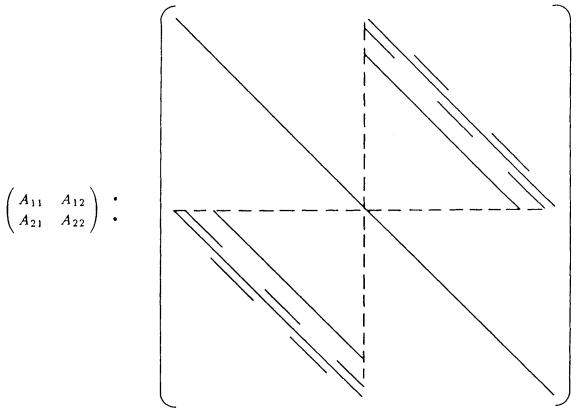

FIGURE 19 Matrix of the eigenvalue problem for $m = 0$.

2.5. *Waveguides and Cavities of Translational Symmetry*

The difference equations for the waveguide problem are similar to those for the deflecting modes. Instead of a certain azimuthal dependence, we have the longitudinal dependence

$$\mathbf{E}(x, y, \Delta z) = \mathbf{E}_0(x, y)e^{i\beta\Delta z}, \tag{16}$$

which is, to a first approximation,

$$\mathbf{E}_0(x, y)(1 + i\beta\,\Delta z), \tag{17}$$

with the propagation constant β. The same is true for cavities that are not cylindrically symmetric but don't change their geometry in the z direction for $0 \le z \le L$, where L is the length of the cavity.

Again Maxwell's equations are written in integral form and discretized in a way fully analogous to the case of deflecting modes (compare appendix) with $(\mathbf{F}', \tilde{\mathbf{F}}') = (\mathbf{E}', \mathbf{B}')$. Then all $\mathbf{B}'$ components and the longitudinal $\mathbf{E}'$ component, E_z, are eliminated. The resulting linear algebraic eigenvalue problem has the squared propagation constants for a given frquency ω as eigenvalues.

This option of URMEL-T renders it possible to compute the functional relationship between the frequency and the propagation constant for, e.g., dielectric-loaded waveguides.

3. SOLUTION OF THE EIGENVALUE PROBLEM

Here, we use the same method as in URMEL.[2,7,8] Since we are only interested in the n lowest eigenvalues, the problem can be solved using a basis transformation which leads to a problem of far fewer dimensions. The matrix of this problem acts over the subspace spanned by the n eigenvectors of the n lowest eigenvalues. This small eigenvalue problem is then solved by a direct conventional method (e.g., an EISPACK routine[9]).

4. EXAMPLES

We will present calculations for several realistic cavities and waveguides with and without material insertions. To check the accuracy, we consider first the pillbox cavity and a spherical cavity where we compare the results of URMEL-T with analytically calculated frequencies and with the results of URMEL.

4.1. *Pillbox Cavity and Sphere*

A detailed error analysis is not given here because of its length. Besides the fineness of the mesh, the quality of the approximation of the cavity geometry influences the error, and this quality depends heavily on the given cavity.

We first choose the pillbox cavity, for which no error due to the approximation of the geometry occurs and for which the exact resonance frequencies are analytically known. In Table I, we compare an URMEL run with N_1 points with an URMEL-T run with N_2 points, where $2N_1$ and $3N_2$ have about the same magnitude (because URMEL-T has three field values associated with each mesh point, while URMEL has two) for the calculation of deflecting modes (compare 2.3 with Ref. 2). These runs used single precision, which gives on IBM about seven decimal digits. It is obvious that the rounding errors overcome the better discretization at some point. If very accurate results are needed, the code can be run in double precision, where the influence of rounding errors is much smaller.

Double precision runs lead to the following relationship between accuracy and the number of mesh points:

$$\left|\frac{\Delta f}{f}\right| \sim \frac{1}{2.2 \cdot N^{1.2}} \tag{18}$$

The dependence of the error upon the number of unknown quantities is also illustrated in Fig. 20 for URMEL-T, as well as for URMEL.

For the spherical cavity, a comparison of URMEL and URMEL-T makes evident the influence that the quality of the geometrical approximation has. This influence obviously depends on the special mesh used. Table II shows a comparison between an URMEL run with N_1 points and an URMEL-T run with N_2 points, where N_1 and $2N_2$ have about the same magnitude (URMEL-T has two azimuthal field values per mesh point while URMEL has one for the calculation of monopole modes—compare Section 2.4 with Ref. 2).

4.2. *Dielectric-Loaded Cavity*

A new feature that URMEL-T offers is the possibility of inserting dielectrics in the cavity. To investigate the accuracy of the program in this regard, we calculated the frequency shift caused by a piece of Teflon in a DORIS cavity (Fig. 21) and compared the results with experimental measurements. The computed frequency shift caused by this Teflon cylinder (dielectric constant $\epsilon_r = 2$) shows

TABLE I

Lowest transverse mode frequencies in a pillbox of radius 1 m and gap length 2 m

Mode	Frequency, MHz[10]	URMEL $2N_1$	URMEL Frequency, MHz	URMEL Error	URMEL-T $3N_2$	URMEL-T Frequency, MHz	URMEL-T Error
TM110	182.82	242	182.17	$-3.6 \cdot 10^{-3}$	216	182.43	$-2.1 \cdot 10^{-3}$
		968	182.67	$-8.2 \cdot 10^{-4}$	864	182.73	$-4.9 \cdot 10^{-4}$
		2178	182.76	$-3.3 \cdot 10^{-4}$	1944	182.76	$-3.3 \cdot 10^{-4}$
		3872	182.79	$-1.6 \cdot 10^{-4}$	3348	182.77	$-3.7 \cdot 10^{-4}$
		6050	182.76	$-3.3 \cdot 10^{-4}$	5016	182.73	$-4.9 \cdot 10^{-4}$
TE110	173.74	6050	173.67	$-4.0 \cdot 10^{-4}$	5016	173.72	$-1.2 \cdot 10^{-4}$

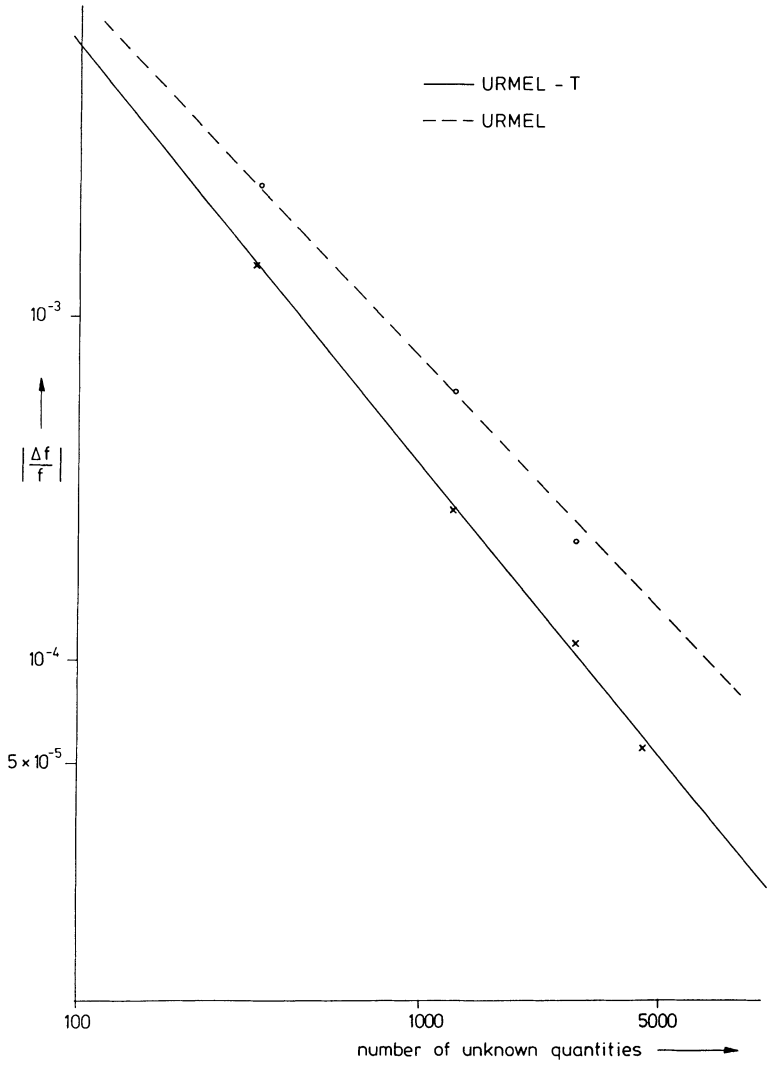

FIGURE 20 Relative error of the frequency, as a function of the number of unknowns.

good agreement with measured data[11] as it can be seen in Table III. The reasonable difference found is due to the slightly modified cavity shape taken for the URMEL-T calculation, where the flanges are left out.

4.3. Waveguide

For a dielectric waveguide, we computed the relation between the frequency ω and the propagation constant β. The highest β's have been computed with

TABLE II

Lowest mode in a spherical cavity of radius 1 m. Due to the spherical symmetry, the mode EE1 with the exact frequency 130.911 MHz[10] can be calculated as TM0-EE-1 or as 1-ME-1; compare Ref. 2 for mode notation

		URMEL			URMEL-T	
Mode	N	Frequency, MHz	Error	$2N$	Frequency, MHz	Error
TM0-EE-1	121	128.972	$-1.5 \cdot 10^{-2}$	144	130.750	$-1.2 \cdot 10^{-3}$
	484	130.733	$-1.4 \cdot 10^{-3}$	576	130.879	$-2.4 \cdot 10^{-4}$
	1089	130.762	$-1.1 \cdot 10^{-3}$	1296	130.892	$1.5 \cdot 10^{-4}$
	1936	130.655	$-2.0 \cdot 10^{-3}$	2232	130.885	$-2.0 \cdot 10^{-4}$
	3025	130.721	$-1.5 \cdot 10^{-3}$	3510	130.929	$+1.4 \cdot 10^{-4}$

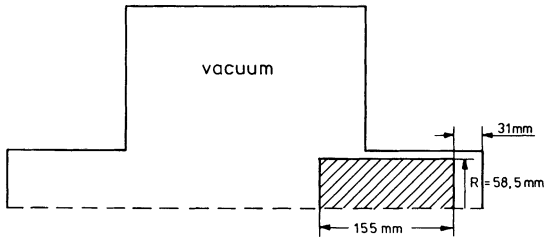

FIGURE 21 Geometry of the dielectric-loaded cavity.

TABLE III

Frequency shift caused by a small Teflon cylinder inserted in a DORIS cavity ($N = 968$)

	Original frequency, MHz		Frequency shift, MHz	
Mode	Calculated	Measured	Calculated	Measured
TM010	498.406	498.488	6.356	6.614
TM011	739.302	745.667	7.419	8.399
TM110	775.286	775.870	4.606	5.980

URMEL-T for different frequencies. The result is illustrated in Fig. 22, which fits a few dozen distinct values of k_0 ($= \omega/c$), each representing a different URMEL-T run. Figure 23 shows a cut through the dielectric waveguide, together with a possible triangular mesh. The corresponding transverse fields for the fundamental mode with frequency 3 GHz are plotted in Fig. 24.

4.4. Multicell Cavity

To simulate the influence of the beam pipe, it is usual to tune the last cell of a multicell cavity: The radius of this cell is modified to achieve a uniform field

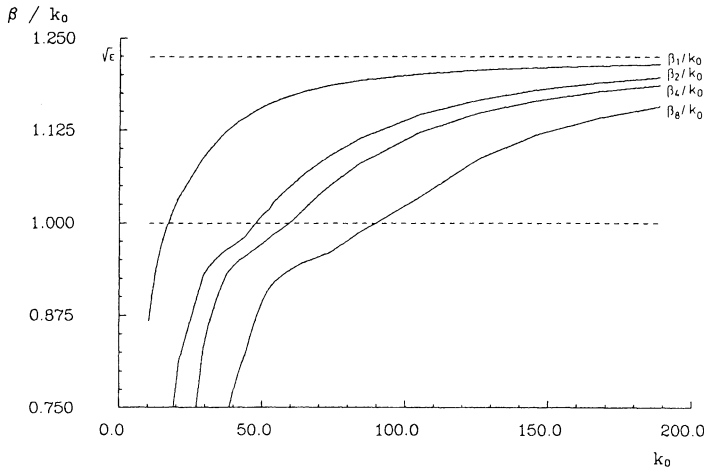

FIGURE 22 Relation between the wave number k_0 $\left(k_0 = \frac{\omega}{c}\right)$ and $\frac{\beta}{k_0}$ for the dielectric-loaded waveguide.

distribution in all cells. The triangular mesh is able to follow even very small deviations between the radii of the middle cells and the outer cell, while a rectangular mesh needs to be very closely spaced to allow the represention of such an input geometry and to fulfill stability requirements. This causes a steeply increasing number of mesh points in rectangular grids for small changes in the radii of only a part of the cells, whereas for the triangular mesh the mesh size may be left unchanged.

To illustrate this fact, we show the tuned 1-GHz PETRA nine-cell superconducting cavity. The radius of the middle cells is 139,595 mm, while the last cell has a radius of 138,345 mm. Figure 25 shows the cavity together with the triangular mesh of 1960 points. To approximate this geometry in a rectangular mesh many more points would be necessary. Figure 26 shows contours of

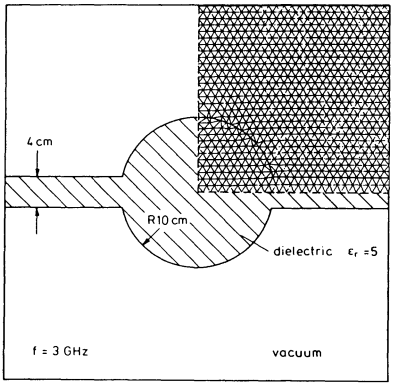

FIGURE 23 Dielectric waveguide with mesh for the part which is essential for a run of URMEL-T.

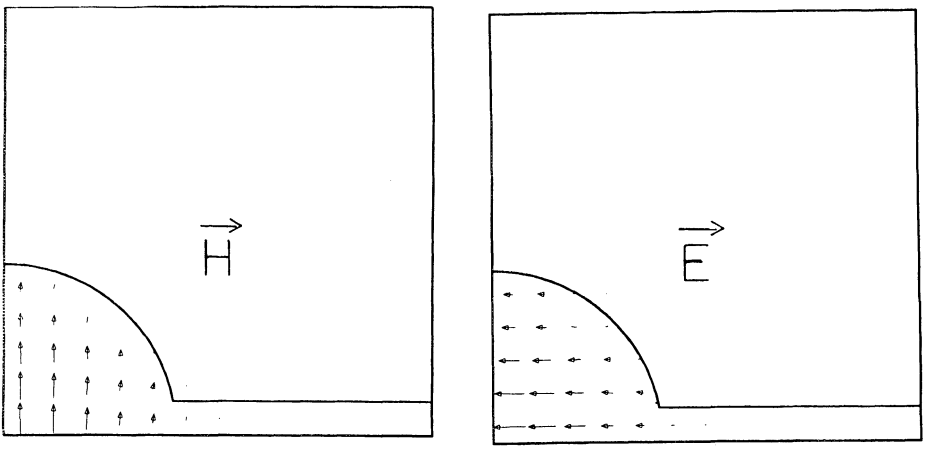

FIGURE 24 Field maps for the fundamental mode.

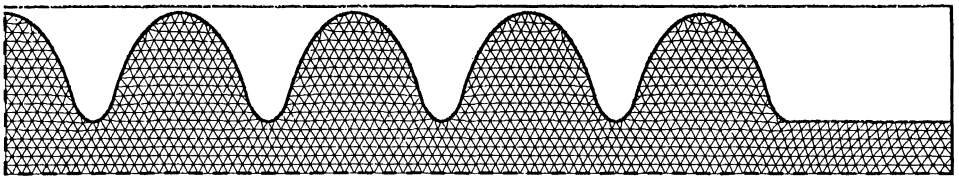

FIGURE 25 Tuned PETRA nine-cell cavity, showing the mesh used.

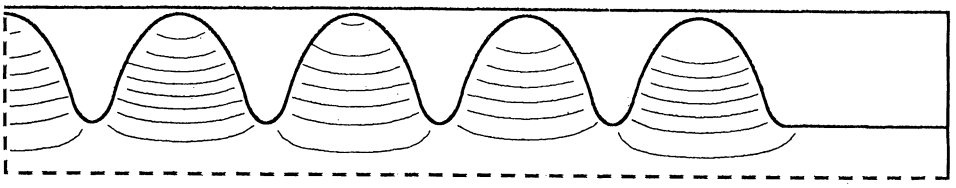

FIGURE 26 Contours of constant $r \cdot H_\varphi$ for the π mode of the tuned nine-cell cavity.

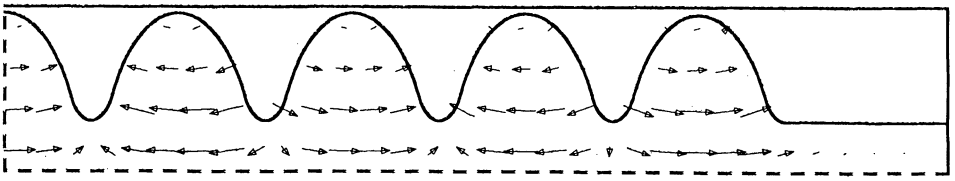

FIGURE 27 Arrow plot of the electric field for the π mode. The measurements gave 1000.1 MHz as frequency; URMEL-T calculated 1007.5 MHz.

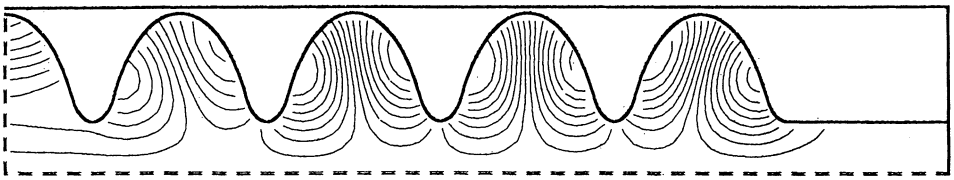

FIGURE 28 Contours of constant $r \cdot H_\varphi$ for the TM011-$8\pi/9$ mode. The measurements gave 1983.7 MHz as frequency; URMEL-T calculated 1975.3 MHz.

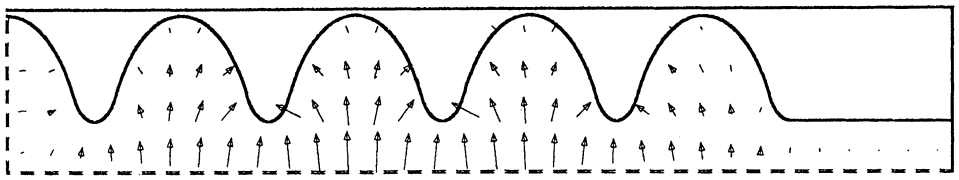

FIGURE 29 Arrow plot of the electric field for the "TE111-$2\pi/9$"-like mode. The measurements gave 1271.2 MHz as frequency; URMEL-T calculated 1289.8 MHz.

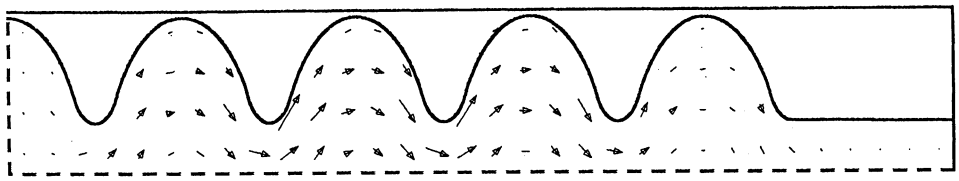

FIGURE 30 Arrow plot of the magnetic field for the "TE111-$2\pi/9$"-like mode.

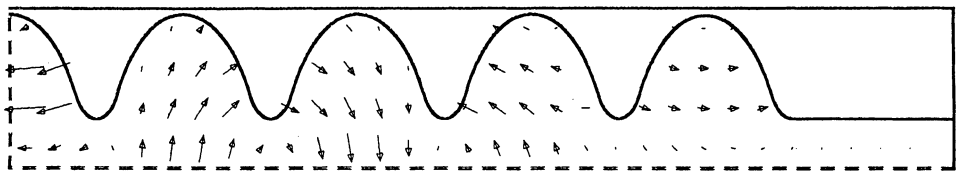

FIGURE 31 Arrow plot of the electric field for the "TM110-$\pi/9$"-like mode. The measurements gave 1428.7 MHz as frequency; URMEL-T calculated 1432.7 MHz.

constant $r \cdot H_\varphi$ of the π mode. These lines show the direction of the electric field. Their density is proportional to $r \cdot \mathbf{E}$. An arrow plot of the electric field of this mode is also shown in Fig. 27. The contours of constant $r \cdot H_\varphi$ of a higher monopole mode can be seen in Fig. 28. Figures 29, 30, and 31 present arrow plots of the electric and magnetic fields of two dipole modes. The calculated frequencies are compared with measured frequencies.[12] The measurements have been done with a cavity with only very small differences in the cavity shape.

5. THE PROGRAM

The code of URMEL-T is available at DESY. The structure of the input data is compatible with that of URMEL. For the features that URMEL-T offers in addition, some new parameters have been introduced. The interface routines (e.g., for plotting) are the same as for URMEL and TBCI,[3] so that the code can be installed easily. More detailed information about the program is given in the user's guide.[13]

6. SUMMARY

The computer code URMEL-T enlarges the two-dimensional scope of application of the FIT discretization method in two directions:

(i) First, it allows the calculation of resonant modes (including the TE0 modes) in cylindrically or translationally symmetric cavities with dielectric and/or permeable insertions, as well as the calculation of propagation constants in waveguides. Herewith, URMEL-T offers a new feature in the domain of computational evaluation of rf fields.

(ii) Second, URMEL-T is well suited to structures with elliptical or circular parts in their geometry, and for tuning multicell cavities. This is based on the properties of a triangular mesh combined with the powerful FIT method. The latter makes sure that the solutions fulfill all Maxwell's equations, i.e., they are physically significant.

URMEL-T thus presents a widely useful extension of the program group for the solution of Maxwell's equations.

REFERENCES

1. T. Weiland, "Eine Methode zur Lösung der Maxwellschen Gleichungen für sechskomponentige Felder auf diskreter Basis", *AEÜ Archiv für Elektronik und Übertragungstechnik* **31,** 116 (1977).
2. T. Weiland, *Nucl. Instrum. Methods* **216,** 329 (1983).
3. T. Weiland, *Particle Accelerators* **15,** 245 (1984), and references therein.
4. T. Weiland, *Design of RF Quadrupoles and RF Waveguides with URMEL* 3.0, DESY HERA report 84-18 (1984).
5. K. Halbach and R. F. Holsinger, *Particle Accelerators* **7,** 213 (1976).
6. A. G. Daikovsky, Yu. I. Portugalov and A. D. Ryabov, *Particle Accelerators* **12,** 59 (1982).
7. J. Tückmantel, *URMEL 1.8, URMEL with a High Speed and High Precision Eigenvector Finder,* CERN/EF/RF 83-5 (1983).
8. J. Tückmantel, *Application of SAP in URMEL,* CERN/EF/RF 85-4 (1985).
9. B. T. Smith *et al., Matrix Eigensystem Routines—EISPACK Guide* (Springer-Verlag, Berlin, 1976).
10. H. Henke, *Spherical Modes,* CERN-ISR-RF/81-29 (1981).
11. A. Zolfaghari, private communication.

12. J. Peters and T. Weiland, *Mode Computation and Measurement of the DESY Nine Cell Superconducting Cavity,* DESY report M-85-02 (1985).
13. C. Palm, U. van Rienen, and T. Weiland, *URMEL and URMEL-T Userguide* (*Modal Analysis of Cylindrically Symmetric Cavities; Evaluation of RF-Fields in Waveguides*), DESY report M-85-11 (1985).

LIST OF SYMBOLS

$\mathbf{E}, \mathbf{H}$	electric and magnetic field
$\mathbf{F}, \tilde{\mathbf{F}}$	field on the triangular and on the dual mesh
$F_{a,k}$	projection of the $\mathbf{F}$ field on the triangle side a attached to mesh node k
$\tilde{F}_{\varphi i,k}$	azimuthal $\mathbf{F}$ field component at triangle i of node k; $i = 1, 2$
Z_0, Y_0	free-space impedance, admittance
ϵ_0	permittivity of the vacuum, $\frac{10^7}{4\pi c^2}$
μ_0	permeability of the vacuum, $4\pi \cdot 10^{-7}$
c	speed of light
ϵ_r	relative permittivity; material constants $\frac{\epsilon}{\epsilon_0}$
μ_r	relative permeability; material constant $\frac{\mu}{\mu_0}$
m	azimuthal mode number, i.e., fields $\alpha \cos m\varphi$ or $\sin m\varphi$
1-EE-4	mode with electric boundary on both sides; dipole. fourth mode found in this subset
2-ME-3	mode with magnetic boundary on the left and electric boundary on the right; quadrupole, third mode found in this subset
k	wave number; $k = \frac{\omega}{c}$
$\mathbf{G}$	triangular mesh
$\mathbf{G_M}$	dual mesh with perpendicular bisectors for sides
$\mathbf{G_S}$	dual mesh with centers of mass of each triangle as (dual) mesh points
i, j	running index for mesh lines/points in r, z (x, y) direction
I, J	number of mesh lines in $r(x)$ direction, number of points [in $z(y)$ direction] on each mesh line in $r(x)$ direction
N	number of mesh points; $N = I \cdot J$
k	as index: mesh point number $k = (i-1) \cdot J + j$
$\alpha_{bc,k,p}$	element of A_{bc}, where p is 0–3, denoting one of the diagonals
$\alpha_{12,k,p}$	element of A_{12}, where p is 0–2, denoting one of the diagonals
A	matrix of the eigenvalue problem
A_{aa}	submatrix connecting F_a and F_a
A_{21}	submatrix connecting $\tilde{F}_{\varphi 2}$ and $\tilde{F}_{\varphi 1}$
$\mathbf{x}$	column vector holding all $\mathbf{F}$ or $\tilde{\mathbf{F}}$ field components
$\mathbf{e}_r, \mathbf{e}_\varphi, \mathbf{e}_z$	unit vector in r, φ, z direction

APPENDIX

The discretization of Maxwell's equations (9) is shown in this chapter. The derivation of the difference equations includes the incorporation of the boundary conditions. To elucidate the principle it is sufficient to consider the case $(\mathbf{F}', \tilde{\mathbf{F}}') = (\mathbf{E}', \mathbf{B}')$.

A.1. Integration for $E_{a,k}$, $E_{b,k}$, and $E_{c,k}$

We integrate

$$\oint \mathbf{H}' \cdot d\mathbf{s} = k \int \epsilon_r \mathbf{E}' \cdot d\mathbf{A}$$

over the area shown in Fig. 32 (for cavities) or Fig. 33 (for waveguides).

A.1.1. Cavities. For cavities,

$$k \cdot E_{a,k} \cdot \cos \alpha_k \cdot (\epsilon_{1,k} \cdot \pi \cdot l_1 \cdot (r_0 + r_1) + \epsilon_{2,k-J} \cdot \pi \cdot l_2 \cdot (r_0 + r_2)) \cdot \int_0^{\psi} \frac{\cos m\varphi}{2\pi} d\varphi$$

$$= \left(B_{\varphi 1,k} \cdot \frac{2\pi r_1}{\mu_{1,k}} - B_{\varphi 2,k-J} \cdot \frac{2\pi r_2}{\mu_{2,k-J}} \right) \cdot \int_0^{\psi} \frac{\cos m\varphi}{2\pi} d\varphi$$

$$- B_{a,k} \cdot \left(\frac{l_1}{\mu_{1,k}} + \frac{l_2}{\mu_{2,k-J}} \right) \cdot \sin m\psi, \quad \text{(A-1)}$$

with $0 < \psi \leq 2\pi$, and α_k is the angle between $E_{a,k}$ and the normal to the plane used for the integration. Thus, letting $\psi \to 0$, we have an equation of the form

$$kE_{a,k} = a_{1,k} B_{\varphi 1,k} - a_{2,k} B_{\varphi 2,k-J} - m a_{3,k} B_{a,k}, \quad \text{(A-2)}$$

with formal coefficients $a_{1,k}$, $a_{2,k}$, and $a_{3,k}$. In the same way, we get linear equations for $E_{b,k}$ and $E_{c,k}$:

$$kE_{b,k} = b_{1,k} B_{\varphi 1,k-1} - b_{2,k} B_{\varphi 2,k} + m b_{3,k} B_{b,k}, \quad \text{(A-3)}$$

$$kE_{c,k} = -c_{1,k} B_{\varphi 1,k} + c_{2,k} B_{\varphi 2,k-1} + m c_{3,k} B_{c,k}, \quad \text{(A-4)}$$

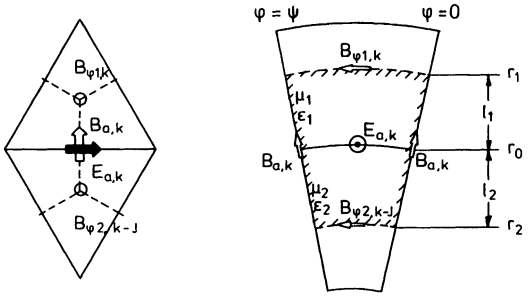

FIGURE 32 Area of integration for $E_{a,k}$ for cavities. The left-hand figure is the mesh drawn in a plane $\varphi = \text{const}$, while the right-hand figure is in the plane used for the integration of $E_{a,k}$.

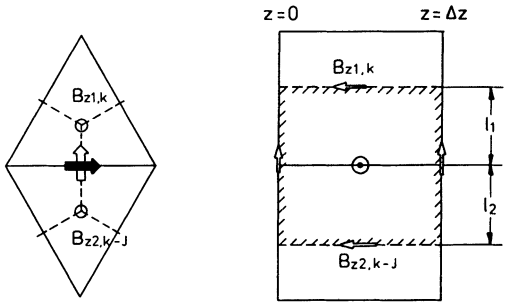

FIGURE 33 Area of integration for $E_{a,k}$ for waveguides. The left-hand figure is drawn in a plane $z = \text{const}$, while the right-hand figure is in the plane used for the integration of $E_{a,k}$.

where the superposed subscripts indicate values to be used for mesh points of type I or II, respectively (upper = type I; see Section 2.1 and Fig. 11).

A.1.2. Waveguides. To first order in Δz, and where α_k is the angle between $E_{a,k}$ and the normal to the integration plane,

$$i \cdot k \cdot E_{a,k} \cdot \cos \alpha_k \cdot (\epsilon_{1,k} \cdot \Delta z \cdot l_1 + \epsilon_{2,k-J} \cdot \Delta z \cdot l_2) = \left(B_{z1,k} \cdot \frac{1}{\mu_{1,k}} - B_{z2,k-J} \cdot \frac{1}{\mu_{2,k-J}}\right) \cdot \Delta z - B_{a,k} \cdot \left(\frac{l_1}{\mu_{1,k}} + \frac{l_2}{\mu_{2,k-J}}\right) \cdot i \cdot \beta \cdot \Delta z. \quad \text{(A-5)}$$

This gives, for $\Delta z \to 0$, an equation of the form

$$ikE_{a,k} = a_{1,k}B_{z1,k} - a_{2,k}B_{z2,k-J} - i\beta a_{3,k}B_{a,k}. \quad \text{(A-6)}$$

Likewise, we get for $E_{b,k}$ and $E_{c,k}$

$$ikE_{b,k} = b_{1,k}B_{z1,k_k^{-1}} - b_{2,k}B_{z2,k} + i\beta b_{3,k}B_{b,k}, \quad \text{(A-7)}$$

$$ikE_{c,k} = -c_{1,k}B_{z1,k} + c_{2,k}B_{z2,k_{k-1}^{k}} + i\beta c_{3,k}B_{c,k}, \quad \text{(A-8)}$$

where again the superposed subscripts denote values to be used depending to the rows of the mesh being considered.

A.2. Integration for $B_{a,k}$, $B_{b,k}$, $B_{c,k}$, $B_{\varphi 1,k}$, and $B_{\varphi 2,k}$

The Maxwell equation

$$\oint \mathbf{E}' \cdot d\mathbf{s} = k \int \mu_r \mathbf{H}' \cdot d\mathbf{A}$$

is integrated over the areas shown in Figs. 34 and 35.

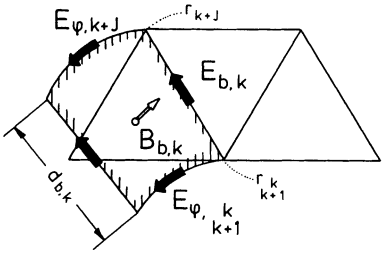

FIGURE 34 Area of integration for $B_{b,k}$ for cavities. The cross-hatched path is perpendicular to the triangular mesh and results from sweeping the mesh through an angle ψ about the z axis.

A.2.1. Cavities. For cavities, we get the following for $B_{b,k}$:

$$k \cdot B_{b,k} \cdot \cos\beta_k \cdot \pi(r_{k+1}^{\ k} + r_{k+J}) \cdot d_{b,k} \cdot \int_0^{\psi} \frac{\sin m\varphi}{2\pi} d\varphi$$
$$= (-E_{\varphi,k+1}^{\ k} \cdot 2\pi \cdot r_{k+1}^{\ k} + E_{\varphi,k+J} \cdot 2\pi \cdot r_{k+J}) \cdot \int_0^{\psi} \frac{\sin m\varphi}{2\pi} d\varphi$$
$$+ E_{b,k} \cdot d_{b,k} \cdot (\cos m\psi - 1), \quad \text{(A.9)}$$

with $0 < \psi \leq 2\pi$. This gives

$$kB_{b,k} = -e_{1,k}E_{\varphi,k+1}^{\ k} + e_{2,k}E_{\varphi,k+J} + me_{3,k}E_{b,k}. \quad \text{(A-10)}$$

The integration area is shown in Fig. 34. Analogously, the equations for $B_{a,k}$ and $B_{c,k}$ are

$$kB_{a,k} = d_{1,k}E_{\varphi,k} - d_{2,k}E_{\varphi,k+1} - md_{3,k}E_{a,k}, \quad \text{(A-11)}$$
$$kB_{c,k} = f_{1,k}E_{\varphi,k+J+1}^{\ k+J} - f_{2,k}E_{\varphi,k} + mf_{3,k}E_{c,k}. \quad \text{(A-12)}$$

A.2.2. Waveguides. To first order in Δz,

$$-i \cdot k \cdot B_{b,k} \cdot \cos\beta_k \cdot \Delta z \cdot d_{b,k}$$
$$= (-E_{z,k+1}^{\ k} + E_{z,k+J}) \cdot \Delta z + E_{b,k} \cdot d_{b,k} \cdot i \cdot \beta \cdot \Delta z. \quad \text{(A-13)}$$

Hence, letting $\Delta z \to 0$, we have for $B_{b,k}$

$$-ikB_{b,k} = -e_{1,k}E_{z,k+1}^{\ k} + e_{2,k}E_{z,k+J} + i\beta e_{3,k}E_{b,k}. \quad \text{(A-14)}$$

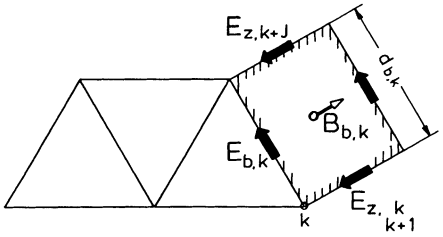

FIGURE 35 Area of integration for $B_{b,k}$ for waveguides. The cross-hatched path is perpendicular to the triangular mesh and results from sweeping the mesh through a distance Δz along the z axis.

The integration area is shown in Fig. 35. Analogously, the equations for $B_{a,k}$ and $B_{c,k}$ are

$$-ikB_{a,k} = d_{1,k}E_{z,k} - d_{2,k}E_{z,k+1} - i\beta d_{3,k}E_{a,k}, \tag{A-15}$$

$$-ikB_{c,k} = f_{1,k}E_{z,k+J}^{k+J+1} - f_{2,k}E_{z,k} + i\beta f_{3,k}E_{c,k}. \tag{A-16}$$

In order to eliminate the azimuthal (or longitudinal) $\mathbf{B}'$ components, we integrate this Maxwell equation over one mesh cell, as illustrated in Fig. 36.

(i) For cavities,

$$k \cdot A_{1,k} \cdot B_{\varphi 1,k} = E_{a,k} \cdot d_{a,k} + E_{b,k}^{k+1} \cdot d_{b,k}^{k+1} - E_{c,k} \cdot d_{c,k}. \tag{A-17}$$

Thus, we get

$$kB_{\varphi 1,k} = g_{1,k}E_{a,k} + g_{2,k}E_{b,k}^{k+1} - g_{3,k}E_{c,k}, \tag{A-18}$$

$$kB_{\varphi 2,k} = h_{1,k}E_{c,k+1}^{k} - h_{2,k}E_{a,k+J} - h_{3,k}E_{b,k}. \tag{A-19}$$

(ii) For waveguides,

$$-i \cdot k \cdot A_{1,k} \cdot B_{z1,k} = E_{a,k} \cdot d_{a,k} + E_{b,k}^{k+1} \cdot d_{b,k}^{k+1} - E_{c,k} \cdot d_{c,k}. \tag{A-20}$$

This gives

$$-ikB_{z1,k} = g_{1,k}E_{a,k} + g_{2,k}E_{b,k}^{k+1} - g_{3,k}E_{c,k}, \tag{A-21}$$

$$-ikB_{z2,k} = h_{1,k}E_{c,k+1}^{k} - h_{2,k}E_{a,k+J} - h_{3,k}E_{b,k}. \tag{A-22}$$

With these equations we can substitute all magnetic quantities in either Eqs. (20)–(22) or (24)–(26).

A.3. Integration for E_φ and E_z

Finally, we want to get a relation between E_φ or E_z and the other electric field components. Since the third Maxwell equation,

$$\iint \epsilon_r \mathbf{E}' \cdot d\mathbf{A} = 0,$$

is automatically fulfilled for time-harmonic fields in the FIT method,[1] we will use this one to obtain the desired relation. This equation is integrated over the

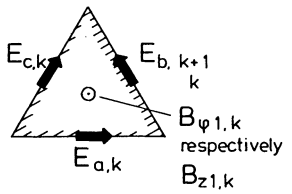

FIGURE 36 Area of integration for $B_{\varphi 1,k}$ or $B_{z1,k}$.

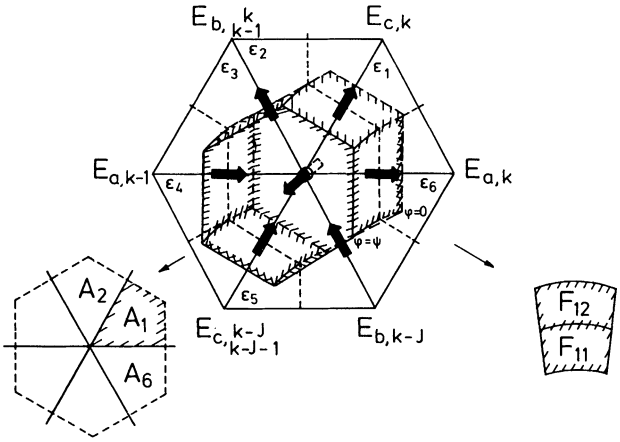

FIGURE 37 Area of integration for $E_{\varphi,k}$ or $E_{z,k}$.

surface shown in Fig. 37 and leads to

$$
\begin{aligned}
&E_{\varphi,k} \cdot (\epsilon_1 A_1 + \epsilon_2 A_2 + \cdots + \epsilon_6 A_6) \sin m\psi \\
&\quad + E_{a,k} \cdot (\epsilon_6 F_{11} + \epsilon_1 F_{12}) \int_0^{\psi} \cos m\varphi \, d\varphi \\
&\quad + E_{c,k} \cdot (\epsilon_1 F_{21} + \epsilon_2 F_{22}) \int_0^{\psi} \cos m\varphi \, d\varphi \\
&\quad + E_{b,k_{-1}^{k}} \cdot (\epsilon_2 F_{31} + \epsilon_3 F_{32}) \int_0^{\psi} \cos m\varphi \, d\varphi \\
&\quad - E_{a,k-1} \cdot (\epsilon_3 F_{41} + \epsilon_4 F_{42}) \int_0^{\psi} \cos m\varphi \, d\varphi \\
&\quad - E_{c,k_{-J-1}^{k-J}} \cdot (\epsilon_4 F_{51} + \epsilon_5 F_{52}) \int_0^{\psi} \cos m\varphi \, d\varphi \\
&\quad - E_{b,k-J} \cdot (\epsilon_5 F_{61} + \epsilon_6 F_{62}) \int_0^{\psi} \cos m\varphi \, d\varphi = 0
\end{aligned}
\tag{A-23}
$$

or

$$
\begin{aligned}
&i \cdot \beta \cdot E_{z,k} \cdot (\epsilon_1 A_1 + \epsilon_2 A_2 + \cdots + \epsilon_6 A_6) \cdot \Delta z \\
&\quad + E_{a,k} \cdot (\epsilon_6 F_{11} + \epsilon_1 F_{12}) \cdot \Delta z + E_{c,k} \cdot (\epsilon_1 F_{21} + \epsilon_2 F_{22}) \cdot \Delta z \\
&\quad + E_{b,k_{-1}^{k}} \cdot (\epsilon_2 F_{31} + \epsilon_3 F_{32}) \cdot \Delta z - E_{a,k-1} \cdot (\epsilon_3 F_{41} + \epsilon_4 F_{42}) \cdot \Delta z \\
&\quad - E_{c,k_{-J-1}^{k-J}} \cdot (\epsilon_4 F_{51} + \epsilon_5 F_{52}) \cdot \Delta z - E_{b,k-J} \cdot (\epsilon_5 F_{61} + \epsilon_6 F_{62}) \cdot \Delta z = 0,
\end{aligned}
\tag{A-24}
$$

which gives the following relation:

$$
mE_{\varphi,k} = -l_{1,k} E_{a,k} - l_{2,k} E_{c,k} - l_{3,k} E_{b,k_{-1}^{k}} + l_{4,k} E_{a,k-1} + l_{5,k} E_{c,k_{-J-1}^{k-J}} + l_{6,k} E_{b,k-J}
\tag{A-25}
$$

or

$$i\beta E_{z,k} = -l_{1,k}E_{a,k} - l_{2,k}E_{c,k} - l_{3,k}E_{b,k_{-1}^{k}} + l_{4,k}E_{a,k-1} + l_{5,k}E_{c,k_{-J-1}^{-J}} + l_{6,k}E_{b,k-J}. \tag{A-26}$$

Using this relation, we finally get Eqs. (10)–(12).